Interfacial Cladding Engineering Suppresses Atomic Thermal Migration to Fabricate Well-Defined Dual-Atom Electrocatalysts

Kunyue Leng, Jianting Zhang, Yi Wang, Dingding Li, Lei Bai, Jingbo Shi, Xiaolin Li, Lirong Zheng, Jinbo Bai, Yunteng Qu

▶ To cite this version:

Kunyue Leng, Jianting Zhang, Yi Wang, Dingding Li, Lei Bai, et al.. Interfacial Cladding Engineering Suppresses Atomic Thermal Migration to Fabricate Well-Defined Dual-Atom Electrocatalysts. Advanced Functional Materials, 2022, 32 (41), ⟨10.1002/adfm.202205637⟩. ⟨hal-05350894⟩

HAL Id: hal-05350894
https://hal.science/hal-05350894v1

Submitted on 6 Nov 2025

Interfacial Cladding Engineering Suppresses Atomic Thermal Migration to Fabricate Well-Defined Dual-Atom Electrocatalysts

Kunyue Leng, Jianting Zhang, Yi Wang, Dingding Li, Lei Bai, Jingbo Shi, Xiaolin Li, Lirong Zheng,* Jinbo Bai,* and Yunteng Qu**

K. Leng, J. Zhang, Y. Wang, D. Li, L. Bai, J. Shi, Y. Qu
International Collaborative Center on Photoelectric Technology and Nano Functional Materials, Institute of Photonics and Photon-Technology, Northwest University, Xi'an, Shaanxi 710069, China
E-mail: yuntengqu@nwu.edu.cn

X. Li
Institute of Intelligent Manufacturing Technology, Shenzhen Polytechnic, Shenzhen 518055, China
E-mail: lixiaolin0427@szpt.edu.cn

L. Zheng
Institute of High Energy Physics, Beijing 100039, China
E-mail: zhenglr@ihep.ac.cn

J. Bai
Université Paris-Saclay, CentraleSupélec, ENS Paris-Saclay, CNRS, LMPS-Laboratoire de Mécanique Paris-Saclay, 8-10 rue Joliot-Curie, Gif-sur-Yvette 91190, France
E-mail: jinbo.bai@centralesupelec.fr

Keywords: dual-atom catalysis, thermal migration, confinement protection, oxygen reduction reaction

Abstract

As an emerging frontier, dual-atom catalysts (DACs) have sparked broad interest in energy catalysis, however the undesired thermal atomic migration during synthesis process pose significant challenge in enabling further applications. Herein, we report an interfacial cladding strategy to construct monodispersed dual-atom metal sites (metal=Fe, Cu or Ir), derived from metal dimer molecule functionalized metal-organic frameworks. First, metal dimer molecule is immobilized at the surface of cubic ZIF-8 by the interfacial cladding of polydopamine, thus preventing the potentially thermal migration of metal atoms during pyrolysis. Then, the paired metal atoms are anchored onto a hollow carbon nanocage and achieve nitrogen coordinated dual-atom metal sites after annealing at 900 °C. Representatively, the resultant dual Fe catalysts exhibit remarkable activity for electrocatalytic oxygen reduction reaction with half-wave potential of 0.951 and 0.816 V in alkaline and acidic media, respectively. Our findings open up an avenue for the rational design of dual-atom catalysts.

1. Introduction

Atomically dispersed catalysts featuring dual metal sites (Dual-Atom catalysts=DACs) have drawn increasing attention due to their unexpected catalytic properties for energy conversion and industrial raw synthesis.[1-3] In comparison to single atom catalysts (SACs) with one metal active site, the synergistic metal active sites in DACs provide more chance to achieve tunable catalytic activity and selectivity. [4-8] Several synthesis strategies have emerged as enabling platform to prepare DACs, including thermal polymerization and precursor-preselected strategy. [9-13] The thermal polymerization methods by precisely thermal control can induce the migration and polymerization of atoms to access dual metal sites. However, the random dispersion of the metal atoms under thermal stimulation generally leads to either low proportion of well-defined dual metal sites or the aggregation into undesired metal clusters or nanoparticles. [14-16] The reported precursor-preselected routes including the immobilization and ligands removal of metal dimer molecule pormises a precisely stratergy to access well-defined DACs. [17-20] But the paired metal atoms contained in dimer molecule will suffer undesired thermal migration under harsh conditions, thus the ligands removal is commonly practised in mild ways, such as photochemical[17] or low temperature.[18,19] Unfortunately, the mild treatment conditions generally result in weak interaction between metal atoms and support, which causes the problems of inadequate stability and activity. Together, although significant development in designing and fabricating DACs has been achieved, the search for a novel strategy to simultaneously suppresses atomic thermal migration and access high-active and stable DACs still remains challenging.

Nano-confined engineering, profiled as suppressing atom migration by the steric hindrance of supports, has been demonstrated a splendid way to prepare stable supported metal catalysts with well-defined structure, even under harsh conditions. [21-25] Herein, inspired by this strategy, we develop an interfacial cladding strategy to suppress atomic thermal migration, which was firstly used to construct monodispersed dual Fe sites. A typical synthetic procedure was shown in **Figure 1a**. Firstly, Fe dimer precursor was immobilized on the surface of CTAB functionalized ZIF-8. Then the as-prepared sample was cladded by polydopamine to prevent undesired thermal atomic migration. After annealing at 900 ^{o}C, paired Fe atom was anchored onto a cubic nanocage, gained well-defined nitrogen coordinated dual Fe sites (Fe_2@PDA-ZIF-900). Remarkably, the as-prepared Fe_2@PDA-ZIF-900 catalysts display superior activity for ORR with half-wave potential of 0.951 V and 0.816 V in alkaline and acidic media, respectively, making it one of the most active non-noble catalysts for ORR. Moreover, this strategy has been confirmed scalable to prepare well-defined Cu_2 and Ir_2 DACs, labeled as Cu_2@PDA-ZIF-900 and Ir_2@PDA-ZIF-900, respectively.

2. Results and Discussion

2.1. Synthesis and characterization

The CTAB functionalized ZIF-8 was prepared according to the previous reported method with slight modification, [26] which exhibited a cubic morphology with a diameter around 260 nm (Figure S1). The Cyclopentadienyliron dicarbonyl dimer was selected as Fe precursor due to its stability under experimental conditions and relatively large molrcule size (Figure S2). After precursor absorption, the FTIR spectra (Figure S3) and color evolution (Figure S4) of samples confirmed the adsorption of Fe_2 dimer molecule onto ZIF-8. Subsequently, the polydopamine layer with thickness around 8 nm was cladded over Fe_2 dimer functioned ZIF-8 (named as PDA@Fe-dimer-ZIF-8) according to TEM analysis (Figure S5). In this case, the ZIF-8 still maintained the original cubic morphology and crystalline texture, as evidenced by XRD pattern and TEM image (Figure S5 and S6). Finally, the annealing at 900 ℃ triggered the decomposition of ZIF-8 and carbonization of polydopamine, resulting in the formation of Fe_2@PDA-ZIF-900. The XPS spectra of C 2p and N 2p uncovered the formation of N-doped carbon carriers after thermal treatment (Figure S7 and S8). It should be noted that the resultant Fe_2@PDA-ZIF-900 catalyst exhibited a morphology of hollow cube around 240 nm (Figure 1b), which can be attributed to the Kirkendall effect.[27] The large specific surface area was demonstrated by N_2 adsorption/desorption test (Figure S9). The Fe content in Fe_2@PDA-ZIF-900 was confirmed to be 1.39 wt% by ICP-OES test, in line with the XPS results (Table S1). EDS element mappings further demonstrated the existence and homogeneous dispersion of Fe element overall carbon framework (Figure 1c).

Aberration-corrected HAADF-STEM is employed to distinguish the atomic distribution of Fe sites, in order to exclude the 3D overlay effects, only the sites at the edge Fe_2@PDA-ZIF-900 were studied. As shown in Figure 1d, a large proportion of paired bright points assigned to Fe atoms were randomly dispersed on N-doped carbon carrier, indicating the formation of diatomic Fe sites. The corresponding intensity profiles highlighted in yellow showed the distance of adjacent Fe atoms was about 2.2 Å (Figure 1e), in line with the previous report.[6] Moreover, no obvious Fe nanoparticles exist based on the HAADF-STEM observations. The XRD patterns further confirmed the absence of diffraction peak for crystalline Fe (Figure 1f). To clarify the coordination environment, Fe_2@PDA-ZIF-900 was further investigated by X-ray absorption spectroscopy (XAFS) in reference to Fe foil, Fe-dimer,FePC and FeO. The X-ray absorption near-edge structure spectra showed white-line intensity of Fe_2@PDA-ZIF-900 located between Fe foil and FeO (Figure 1g), indicating the oxidation state of Fe situated between 0 to +2. This matched well with the Fe 2p XPS analysis (Figure S10). Furthermore, the R-space results showed the first dominant peak of Fe_2@PDA-ZIF-900 resembles FeCp at 1.41 Å (Figure 1h), indicating the Fe-N coordination. More importantly, a secondary peak was detected at 2.20 Å for Fe_2@PDA-ZIF-900, which can be assigned to Fe-Fe bonds, in consistent with HAADF-STEM results.[6, 21] The fitting result at R-space revealed the Fe_2N_6 configuration in Fe_2@PDA-ZIF-900, further excluding the formation of Fe nanoparticles or clusters (Figure 1i and Table S2). Moreover, when the PDA coating process was omitted, particles were detected obviously over the resultant Fe_2@ ZIF-900 after thermal treatment, clarifing that PDA cladding is crucial to prevent thermal migration of metal. (Figrue S11). Together, the interfacial cladding strategy can effectively suppress the atomic thermal migration of Fe_2 precursors, thereby demonstrating it as feasible to construct DACs.

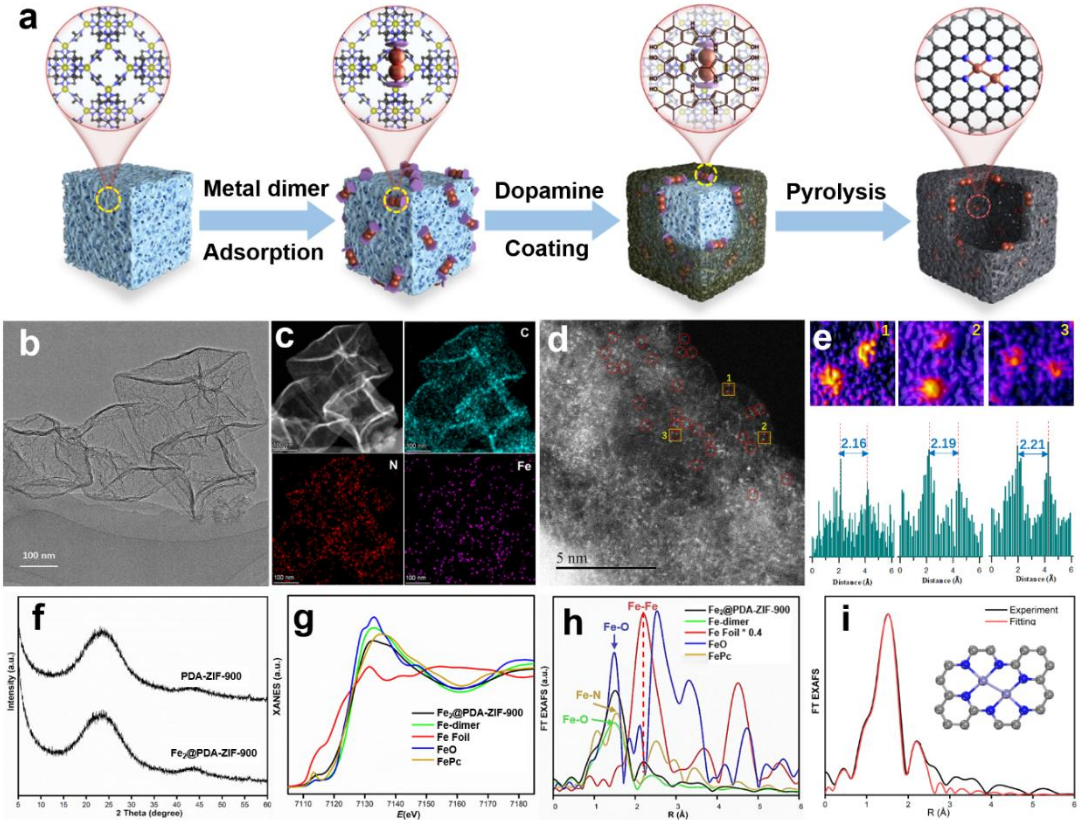

Figure 1. (a) Schematic illustration for preparing dual-atom metal catalysts. (b-i) characterizations of Fe_2@PDA-ZIF-900. (b) TEM image, (c) HAADF-TEM and EDS elemental mapping profiles with C, N and Fe, (d) aberration-corrected HAADF-STEM image,

(e) intensity profiles highlighted in yellow in h, (f) XRD pattern, (g, h) Fe K edge XANES and FT EXAFS spectra, (i) FT EXAFS fitting spectrum at R space.

To further verify the universality of the strategy, we employed different metal precursor (Cu dimer and Ir dimer) to fabricate DACs of Cu_2@PDA-ZIF-900 (**Figure 2a**, b and Figure S12a, S13) and Ir_2@PDA-ZIF-900 (Figure 2e, f and Figure S12b, S14). In HAADF-STEM images (Figure 2c and g), a large proportion of paired bright spots were observed, revealing the formation of dual atoms metal sites. The corresponding intensity profiles confirmed the distance of adjacent Cu atoms and Ir atoms were around 2.3 and 2.6 Å, respectively (Figure 2d and h). EXAFS spectra were employed to further confirm the coordination structure of the as-obtained samples (Figure 2i-m). With regarding to the R space results (Figure 2j and m), the first dominant peaks were detected at 1.44 Å for Cu_2@PDA-ZIF-900 and 1.54 Å for Ir_2@PDA-ZIF-900, suggesting the priority of metal-nitrogen coordination in these samples. Moreover, secondary peaks were found in Cu_2@PDA-ZIF-900 (2.26 Å) and Ir_2@PDA-ZIF-900(2.35 Å), which attributed to Cu-Cu and Ir-Ir coordination, respectively. These results revealed that dual copper and iridium atoms were anchored on nitrogen-doped carbon nanocage.

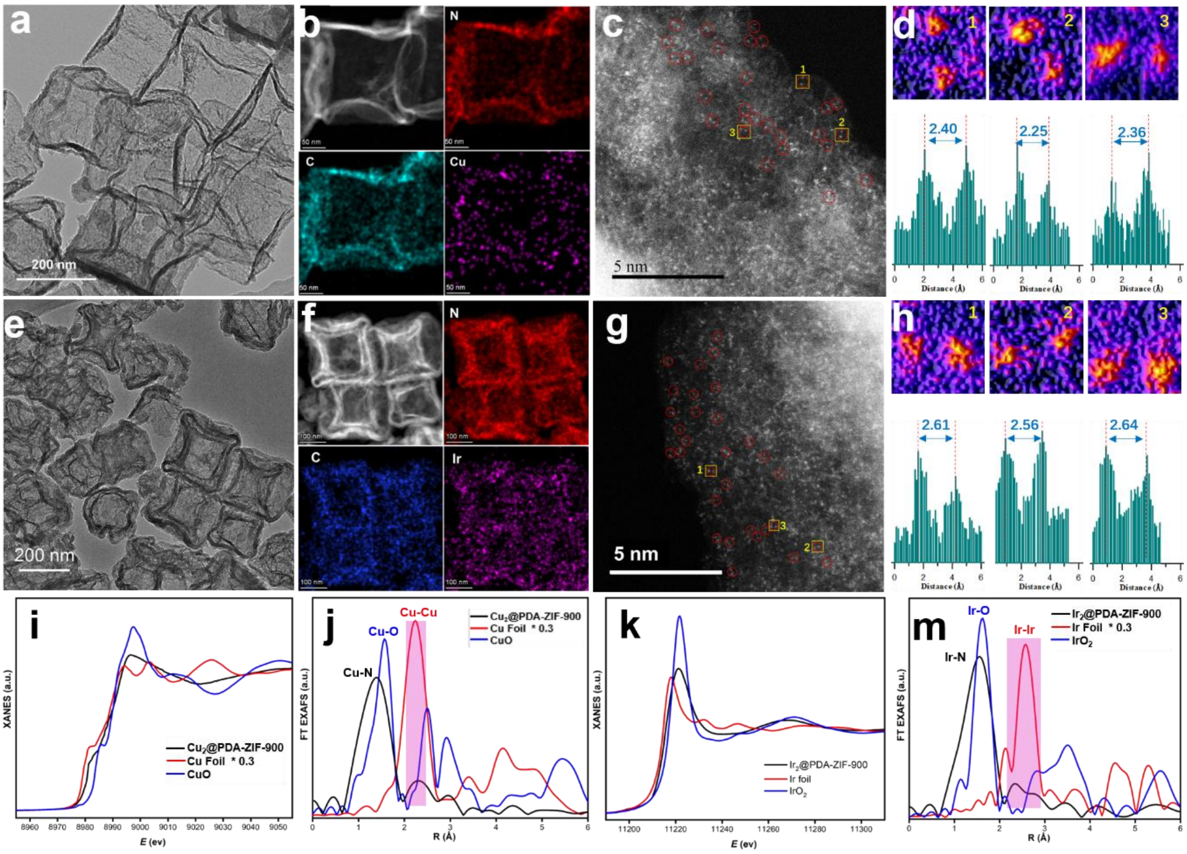

Figure 2. TEM image, HAADF-TEM and EDS elemental mapping profiles, aberration-corrected HAADF-STEM image, intensity profiles highlighted in yellow for Cu_2@PDA-ZIF-

900 (a-d) and for Ir_2@PDA-ZIF-900 (e-h). (i, j) Cu K edge XANES and FT EXAFS spectra of Cu_2@PDA-ZIF-900. (k, m) Ir L_3 edge XANES and FT EXAFS spectra of Ir_2@PDA-ZIF-900.

2.2. Electrochemical Oxygen Reduction Reaction

We investigated the electrocatalytic oxygen reduction reaction (ORR) activity of as-prepared Fe_2@PDA-ZIF-900 considering their merits in splitting O-O bonding, which is crucial for triggering 4 e^- ORR towards H_2O. The ORR activity of Fe_2@PDA-ZIF-900 was evaluated in O_2-saturated 0.1 M KOH, with the Fe_2@ZIF-900, Pt/C, Fe_1@PDA-ZIF-900, Fe nanoparticle@CN (Figure S15), PDA-ZIF-900 as references. Specially, the Fe single atom catalyst (Fe_1@PDA-ZIF-900) was prepared with the similar approach for preparing Fe_2@PDA-ZIF-900, of which the atomically dispersed Fe sites and the FeN_4 coordination structure was demonstrated by HAADF-STEM and XAFS spectra, as well as other characterizations (Figure S16-20).

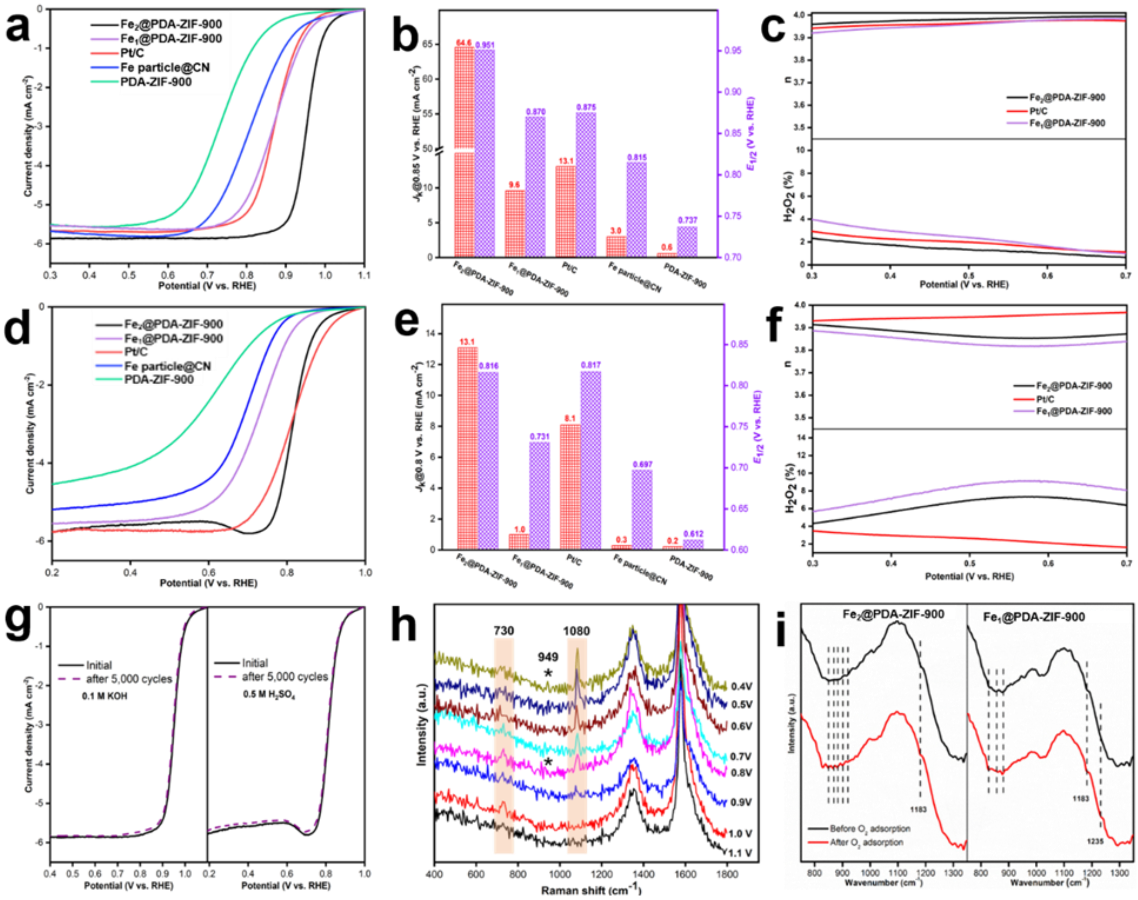

Figure 3. (a) Linear sweep voltammetry (LSV) curves, (b) kinetic current density (J_k) and half-wave potential ($E_{1/2}$), (c) electron transfer number and H_2O_2 yield of Fe_2@PDA-ZIF-900 and references in O_2-saturated 0.1 M KOH solution. (d-f) Results of the above tests in 0.5 M H_2SO_4 solution. (g) LSV curves of Fe_2@PDA-ZIF-900 in alkaline/acid medium before and

after 5000 potential cycles. (h) Potential-dependent operando Raman spectra in O_2-saturated 0.1 M KOH and (i) O_2 absorption in situ DRFTIR spectra of Fe_2@PDA-ZIF-900.

As shown in **Figure 3a**-b and Figure S21, the superior ORR performance of Fe_2@PDA-ZIF-900 was confirmed by a remarkable half-wave potential ($E_{1/2}$) of 0.951V, 60 mV, 80 mV, 76 mV and 136 mV higher than that of Fe_2@ZIF-900 (0.891V), Fe_1@PDA-ZIF-900 (0.871V), Pt/C catalyst (0.875 V) and Fe nanoparticle@CN (0.815 mV), respectively, and superior to those of the most reported non-precious catalysts (Table S3). Furthermore, the poor activity of PDA-ZIF-900 suggested the excellent ORR activity of Fe_2@PDA-ZIF-900 derived from dual Fe sites. The kinetic current density (J_k) for Fe_2@PDA-ZIF-900 (at 0.85 V) was 64.6 mA cm^{-2}, 4.9 times higher than that for Pt/C (Figure 3b). Moreover, the lower Tafel slope of Fe_2@PDA-ZIF-900 (47 mV dec^{-1}) indicated faster dynamics for ORR (Figure S22), in agreement with its smaller charge transfer resistance (Figrue S23). The rotating ring disk electrode (RRDE) measurement in conjunction with Koutecky–Levich (K–L) plots revealed a nearly four-electron ORR pathway for Fe_2@PDA-ZIF-900 (Figure 3c and S24). Notably, low H_2O_2 yield with 2.5 % or below was observed over Fe_2@PDA-ZIF-900, arising from the strong ability of dual Fe sites for breaking O-O bonding.

Moreover, Fe_2@PDA-ZIF-900 also displayed superior ORR performance in acid media. Figure 3d and 3e showed the $E_{1/2}$ of Fe_2@PDA-ZIF-900 was measured as 0.816 V, which is comparable to commercial Pt/C (0.817 V). The Fe_2@PDA-ZIF-900 process a Tafel slope of 63.3 mV dec^{-1}, lower than that of Pt/C (85.1 mV dec^{-1}, Figure S25), suggesting the favorable ORR kinetics. In addition, Fe_2@PDA-ZIF-900 exhibited high J_k with 13.1 mA cm^{-2} (0.8 V), 61% over Pt/C (8.1 mA cm^{-2}). The RRDE measurement disclosed nearly four-electron ORR pathway of Fe_2@PDA-ZIF-900 in 0.5M H_2SO_4 (Figure 3f), the H_2O_2 yield just slightly higher than Pt/C. The stability is also an important factor to evaluated catalyst. Thus, the accelerated durability tests (ADTs) for Fe_2@PDA-ZIF-900 were conducted in O_2-saturated 0.1 M KOH and 0.5 M H_2SO_4. As shown in Figure 3g, no significant decay of $E_{1/2}$ was observed after 5000 cycles. Furthermore, we adopt XPS, XAFS and HAADF-STEM to probe the stability of Fe_2@PDA-ZIF-900 after durability testing. As shown in Figure S26, the used Fe_2@PDA-ZIF-900 still maintained the structure of paired Fe atoms with Fe-Fe bond length of 2.20 Å, indicating its robust electrochemical stability.

2.3. Operando Electrochemical Raman and in-situ DRFTIR

Electrochemical operando Raman spectra was used to investigated the ORR pathway in O_2-saturated 0.1 M KOH (Figure S27). Figure 3h displayed the potential dependent Raman spectra of Fe_2@PDA-ZIF-900. At an initial potential of 1.1 V, no extra signal was detected but the signal of N-doped carbon substance. When the applied potential was shifted to 1.0 V, a band belonged to O-O stretch of *OOH emerged at 730 cm^{-1}, [28, 29] in good agreement with the ORR onset potential (Figure 3a). Negatively shifting the applied potential to 0.9 V, extra band belong to *OH was detected at 1080 cm^{-1},[29] due to the decomposition of *OOH. Further continuously shifting potential from 0.9 to 0.4 V, the intensity of bands at 1080 cm^{-1} increased obviously, while the bands at 730 cm^{-1} were hard to detected. These results suggested the rapid decomposition of *OOH group over Fe_2@PDA-ZIF-900, greatly expediting ORR kinetics.

The fast splitting of O-O bonding could be attributed to the unique O_2 absorption models on dual Fe sites. As comparison, we also investigated the operando Raman test for Fe_1@PDA-ZIF-900 with single Fe site (Figure S28). It is noted that the peroxo-like O_2 species were observed over Fe_2@PDA-ZIF-900 (949 cm^{-1}),[30] while the Fe_1@PDA-ZIF-900 displayed the superoxol-like adsorbed O_2 at 1171 cm^{-1}.[30] This result was further confirmed by in situ DRFTIR spectra (Figure 3i). After O_2 absorption, accessory peaks at 800-950 cm^{-1} belonging to vibrations peroxo-like O_2 species were observed on Fe_2@PDA-ZIF-900.[11] For Fe_1@PDA-ZIF-900, a band assigned to vibrations of superoxo-like O_2 species was detected at 1235 cm^{-1} after O_2 absorption,[11] but the band within the scope of 800-950 cm^{-1} remained identical before and after O_2 absorption. These observations provide strong evidence for the modulation of O_2 absorption configurations on single or dual Fe sites.

2.4. DFT calculations

DFT calculations were performed to further clarify the mechanism of the superior ORR performance over Fe_2@PDA-ZIF-900. Based on the O_2-adsorption energy analysis, peroxo-like O_2 and superoxol-like O_2 species appear to be the optimized models on Fe_2@PDA-ZIF-900 and Fe_1@PDA-ZIF-900 (**Figure 4a**), respectively, in line with the in-situ DRFTIR and Raman results. Furthermore, O-O length of superoxol-like O_2 species turned be elongated to 1.49 Å, compared with that of superoxol-like O_2 species (1.35 Å), indicating the more efficient O-O activation capacity of Fe_2@PDA-ZIF-900 than Fe_1@PDA-ZIF-900.[11] Interestingly, when a hydrogen atom was added onto the O-O bonging of model (i) to simulate ORR pathway,[31] the resultant *OOH rapidly decomposed into O* and *OH over Fe_2@PDA-ZIF-900 (Video1 in SI), which consistent with Raman spectra. The above results confirmed again that the superior ORR performance of Fe_2@PDA-ZIF-900 stems from its excellent O-O activation ability, which was further dementrated by the free-energy evolution diagram of Fe_2@PDA-ZIF-90 and Fe_1@PDA-ZIF-90 (Figure S29).

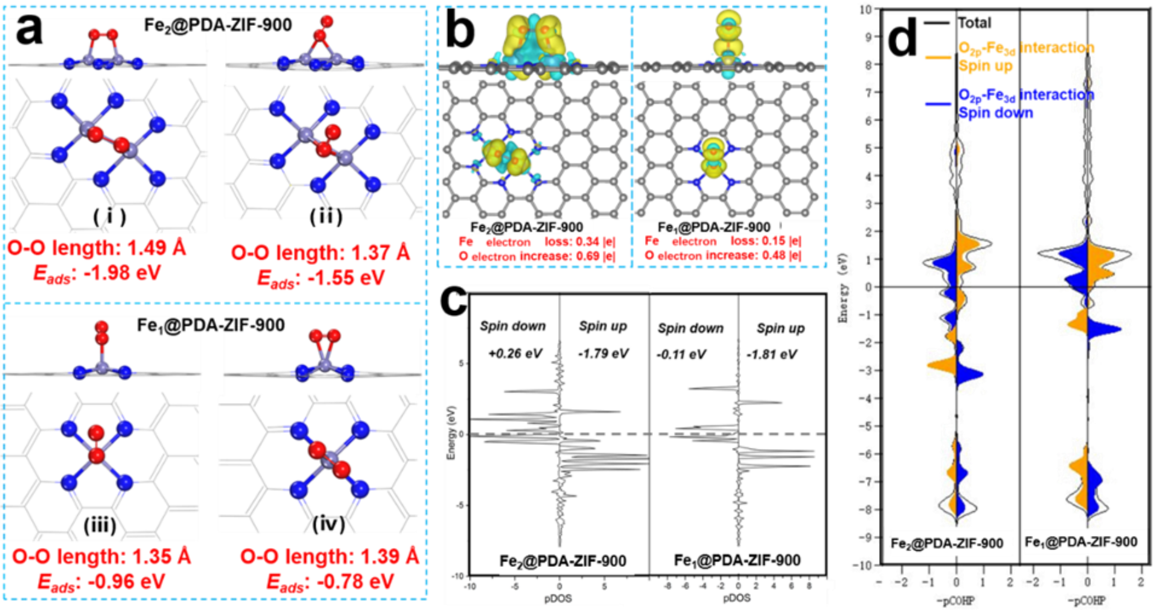

Figure 4. DFT investigations of Fe_2@PDA-ZIF-900 and Fe_1@PDA-ZIF-900. (a) O_2 adsorption models, (b) differential charge density after O_2 adsorption, (c) projected density of states (PDOS) of Fe-d orbitals, (d) crystal orbital Hamilton population (COHP) after O_2 adsorption.

The electronic evolution analysis was also presented to further probe the crucial of dual Fe sites in O-O bonding activation, reference to single Fe sites. Differential charge density and Bader charge disclosed higher |e| transfer from Fe sites to adsorbed O_2 over Fe_2@PDA-ZIF-900 than that over Fe_1@PDA-ZIF-900 (Figure 4b and Table S4). This could be attributed to the decreased antibonding orbitals filling of Fe_2@PDA-ZIF-900, which confirmed by the more positive average d-band center of Fe_2@PDA-ZIF-900 (-0.77) than Fe_1@PDA-ZIF-900 (-0.96) based on PDOS (Figure 4c and Figure S30).[32] Eventually, stronger interaction between Fe sites and O was enabled over Fe_2@PDA-ZIF-900 in Figure 4d (|iCOHP| = 2.96*2 and 3.74 for dual and single Fe sites, respectively).

3. Conclusion

In summary, we developed an interfacial cladding strategy with the aim of suppressing the atomic thermal migration for fabricating stable dual-atom metal catalysts. Accordingly, well-defined Fe_2, Cu_2 and Ir_2 sites were successfully constructed, identified by XAFS and HAADF-STEM. Combining electrochemical evaluation with in situ spectroscopy, as well as theoretical calculation, we revealed that the well-defined dual Fe sites could efficient active

O-O bonding, eventually promoting the ORR performance with 4 e^- pathway. This work provides a new process for the rational design of DACs for further applications.

4. Experimental Section

See the Supporting Information for details of the materials and methods.

Supporting Information

Supporting Information is available from the Wiley Online Library or from the author.

Acknowledgements

We thank the photoemission endstation beamline 1W1B station in the Beijing Synchrotron Radiation Facility (BSRF) for help with the characterizations. This work is financially supported by the National Natural Science Foundation of China (21902150, 51873174 and 52105307), Natural Science Basic Research Program of Shaanxi (2022JQ-082 and 2022JM-018) and China Postdoctoral Science Foundation (2020M673461).

Received: ((will be filled in by the editorial staff))
Revised: ((will be filled in by the editorial staff))
Published online: ((will be filled in by the editorial staff))

References

[1] C. Hou, H. Wang, C. Li and X. Qiang, *Energy Environ. Sci.* **2020,** *13*, 1658-1693.

[2] T. Cui, Y. Wang, T. Ye, J. Wu, Z. Chen, J. Li, Y. Lei, D. Wang and Y. Li, *Angew. Chem. Int. Ed.* **2022**, *61*, DOI: 10.1002/anie. 202115219.

[3] T. Ding, X. Liu, Z. Tao, T. Liu, T. Chen, W. Zhang, X. Shen, D. Liu, S. Wang, B. Pang, D. Wu, L. Cao, L. Wang, T. Liu, Y. Li, H. Sheng, M. Zhu and T. Yao, *J. Am. Chem. Soc.* **2021**, *143*, 11317-11324.

[4] L. Xin, Y. Jiao, Y. Zheng, K. Davey and S. Z. Qiao, *J. Mater. Chem. A* **2019**, *7*, 3648-3654.

[5] J. Yang, W. Li, K. Xu, S. Tan, D. Wang and Y. Li, *Angew. Chem. Int. Ed.* **2022**, DOI: 10.1002/anie.202200366.

[6] S. Tian, Q. Fu, W. Chen, Q. Feng, Z. Chen, J. Zhang, W. Cheong, R. Yu, L. Gu, J. Dong, J. Luo, C. Chen, Q. Peng, C. Draxl, D. Wang and Y. Li, *Nat. Commun*. **2018**, *9*, 2353.

[7] F. Kong, R. Si, N. Chen, Q. Wang, J. Li, G. Yin, M. Gu, J. W, L. Liu and X. Sun, *Appl. Catal. B: Environ.* **2022**, *301*, 120782.

[8] H. Yan, Y. Lin, H. Wu, W. Zhang, Z. Sun, H. Cheng, W. Liu, C. Wang, J. Li, X. Huang, T. Yao, J. Yang, S. Wei and J. Lu, *Nat. Commun*. **2017**, *8*, 1070.

[9] R. Li and D. Wang, *Adv. Energy Mat.* **2022**, 2103564.

[10] Z. Zeng, L. Gan, H. Yang, X. Su, J. Gao, W. Liu, H. Matsumoto, J. Gong, J. Zhang, W, Cai, Z. Zhang, Y. Yan, B. Liu and P. Chen, *Nat. Commun*. **2021**, *12*, 4088.

[11] W. Ye, S. Chen, Y. Lin, L. Yang, S. Chen, X. Zheng, Z. Qi, C. Wang, R. Long, M. Chen, J. Zhu, P. Gao, L. Song, J. Jiang and Y. Xiong, *Chem* **2019**, *5*, 2865-2878.

[12] L. Ma, J. Li, Z. Zhang, H. Yang, X. Mu, X. Gu, H. Jin, D. Chen, S. Yan, S. Liu and S. Mu, *Nano. Research* **2022**, *15*, 1966-1972.

[13] T. He, A. Santiago, Y. Kong, M. Ahsan, R. Luque, A. Du and H. Pan, *Small* **2021**, 2106091.

[14] L. Bai, C. Hsu, D. Alexander, H. Chen and X. Hu, *J. Am. Chem. Soc.* **2019**, *141*, 14190–14199.

[15] Y. Yang, Y. Qian, H. Li, Z. Zhang, D. Do, B. Zhou, J. Dong, W. Yan, Y, Qin, L. Fang, R. Feng, J. Zhou, P. Zhang, J. Dong, G. Yu, Y. Liu, X. Zhang, and X. Fan, *Sci. Adv.* **2020**, *6*, DOI: 10.1126/sciadv. aba6586.

[16] Y. Wang, B. J. Park, V. K. Paidi, R. Huang, Y. Lee, K. Noh, K. Lee, and J. W. Han, *ACS Energy Lett.* **2022**, *7*, 640-649.

[17] Y. Zhao, K. Yang, Z. Wang, X. Yan, S. Cao, Y. Yei, Q. Dong, X. Zhang, J. Thorne, L. Jin, K. Materna, A. Trimpalish, H. Bai, S. Fakra, X. Zhong, P. Wang, X. Pang, J. Guo, M. Flytzani-Stephanopoulos, G. Brudvig, V. Batista and D. Wang, *PANS* **2018**, *115*, 2902-2907.

[18] S. Tian, B. Wang, W. Gong, Z. He, Q. Xu, W. Chen, Q. Zhang, Y. Zhu, J. Yang, Q. Fu, C. Chen, Y. Bu, L. Gu, Xi. Sun, H. Zhao, D. Wang and Y. Li, *Nat. Commun*. **2021**, *12*, 3181.

[19] N. Zhang, X. Zhang, Y. Kang, C. Ye, R. Jin, H. Yan, R. Lin, J. Yang, Q. Xu, Y. Wang, Q. Zhang, L. Gu, L. Liu, W. Dong, J. Liu, D. Wang and Y. Li, *Angew. Chem. Int. Ed.* **2021**, *60*, 13388-13393.

[20] N. Zhang, T. Zhou, J. Ge, Y. Lin, Z. Du, C. Zhong, W. Wang, Q. Jiao, R. Yuan, Y. Tian, W. Chu, C. Wu and Y. Xie, *Matter* **2020**, *3*, 1-13.

[21] Y. Wei, L. Sun, M. Wang, J. Hong, L. Zou, H. Liu, Yu Wang, M. Zhang, Z. Liu, Y. Li, S. Horike, K. Suenaga and Q. Xu, *Angew. Chem. Int. Ed.* **2020**, *59*, 16013-16022.

[22] D. Yu, Y. Ma, F. Hu, C. Lin, L. Li, H. Chen, X. Han and S. Peng, *Adv. Energy Mater.* **2021**, *11*, 2101242.

[23] Z. Zhang, J. Sun, F. Wang and L. Dai, *Angew. Chem. Int. Ed.* **2018**, *57*, 9038-9043.

[24] L. Yu, D. Deng and X. Bao, *Angew. Chem. Int. Ed.* **2020**, *59*, 15294-15297.

[25] A. M. Abdel-Mageed, B. Rungtaweevoranit, M. Parlinska-Wojtan, X. Pei, O. M. Yaghi and R. J. Behm, *J. Am. Chem. Soc.* **2019**, *141*, 5201−5210.

[26] H. Hu, B. Guan and X. W. Lou, *Chem* **2016**, *1*, 102-113.

[27] X. W. Lou, L. Archer and Z. Yang, *Adv. Mat.* **2008**, *20*, 3987-4019.

[28] M. Jiang, C. Fu, R. Cheng, W. Zhang, T. Liu, R. Wang, J. Zhang, and B. Sun, *Adv. Sci.* **2020**, *7*, 2000747.

[29] J. Dong, X. Zhang, V. Briega-Martos, X. Jin, J. Yang, S. Chen, Z. Yang, D. Wu, J. Feliu, C. Williams, Z. Tian and J. Li, *Nat. Energy* **2019**, *4*, 60-67.

[30] Y. Huang, P. Kooyman and M. Koper, *Nat. Commun.* **2016**, *7*, 12440.

[31] J. Wang, W. Liu, G. Luo, Z. Li, C. Zhao, H. Zhang, M. Zhu, Q. Xu, X. Wang, C. Zhao, Y. Qu, Z. Yang, T. Yao, Y. Li, Y. Lin, Y. Wu and Y. Li, *Energy Envrion. Sci,* **2018**, *11*, 3375-3379.

[32] Z. Wang, X. Jin, C. Zhu, Y. Liu, H. Tan, R. Ku, Y. Zhang, L. Zhou, Z. Liu, S. Hwang and H. Fan, *Adv. Mater.* **2021**, 2104718.

An interfacial cladding engineering was developed to suppress atomic thermal migration for fabricating well defined dual-atom metal sites onto hollow carbon nanocage, including Fe_2, Cu_2 and Ir_2 sites. The resultant dual-atom Fe sties exhibit remarkable ORR activity with half-wave potential of 0.951 and 0.816 V in alkaline and acidic media, respectively, due to the efficient O-O bonding activation ability.

K. Leng, J. Zhang, Y. Wang, D. Li, L. Bai, J. Shi, X. Li,* L. Zheng,* J. Bai,* and Y. Qu*

Interfacial Cladding Engineering Suppresses Atomic Thermal Migration to Fabricate Well-Defined Dual-Atom Electrocatalysts